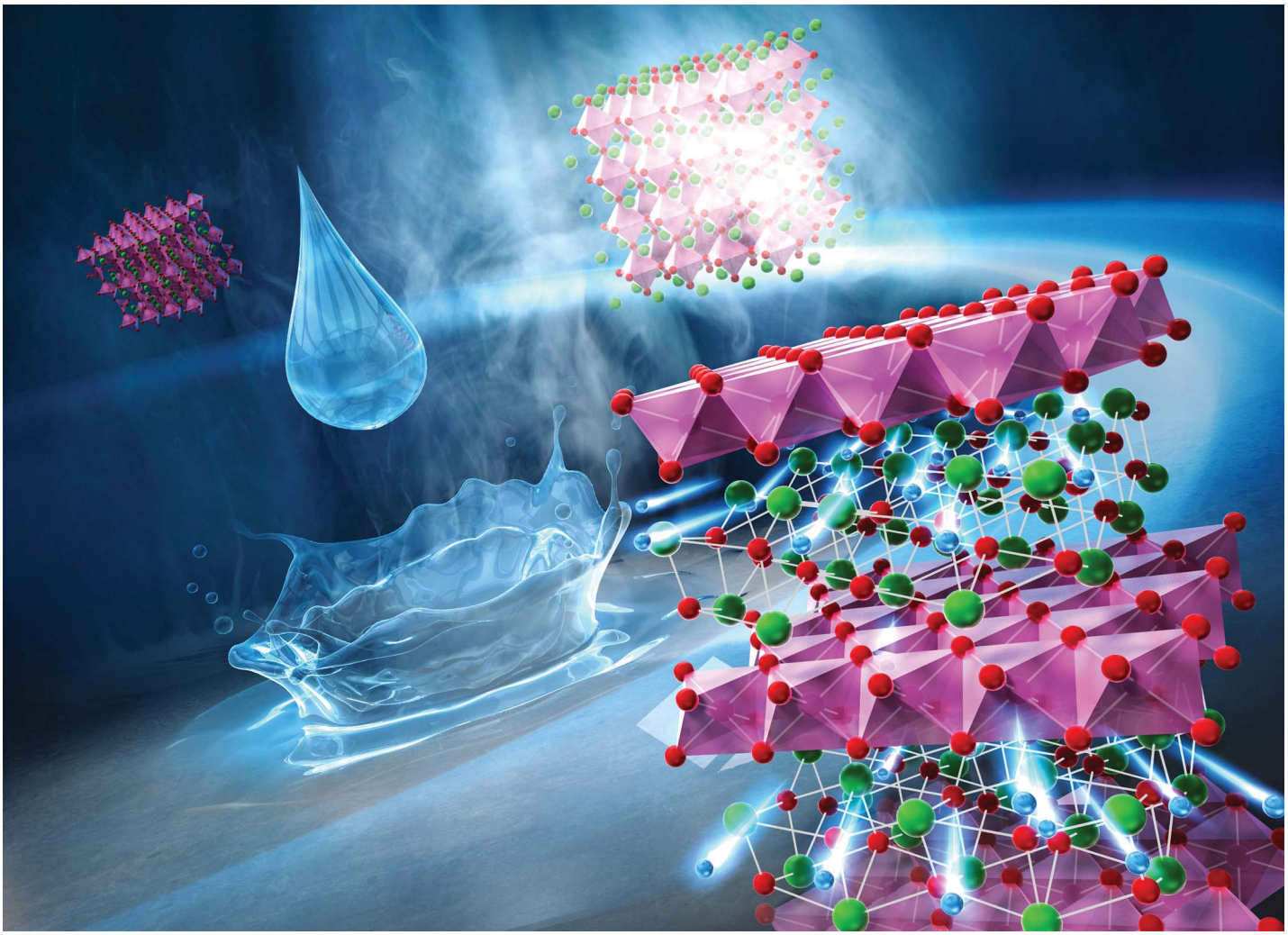

Showcasing research from Professor Teruki Motohashi's laboratory, Department of Applied Chemistry, Kanagawa University, Japan.

Thermally stable proton-conducting oxy-hydroxides synthesized in concentrated water vapor

The innovative synthesis method—"*vapor hydroxidation*"—using high-temperature treatment in concentrated water vapor yields a thermally stable, proton-conducting oxy-hydroxide, $[Ba_2O_x(OH)_y]_{0.55}InO_2$, featuring a unique misfit-layered structure. Image reproduced by permission of Teruki Motohashi from *J. Mater. Chem. A*, 2025, **13**, 21472.

As featured in:

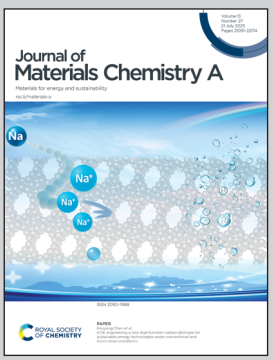

See Miwa Saito, Teruki Motohashi *et al.*, *J. Mater. Chem. A*, 2025, **13**, 21472.

ROYAL SOCIETY OF CHEMISTRY

rsc.li/materials-a

Registered charity number: 207890

Journal of Materials Chemistry A

ROYAL SOCIETY OF CHEMISTRY

PAPER

View Article Online
View Journal | View Issue

Check for updates

Cite this: J. Mater. Chem. A, 2025, 13, 21472

Thermally stable proton-conducting oxy-hydroxides synthesized in concentrated water vapor†

Kenji Arai, [a] Yoko Kokubo, [a] Yusuke Asai, [a] Satoshi Ogawa, [a] Miwa Saito, *[a] Maria Kirsanova, [bc] Iaroslava Shakhova, [c] Artem Abakumov, [b] Fumitaka Takeiri, [d] Hiroshi Kageyama [e] and Teruki Motohashi *[a]

The diverse functionalities of (oxy-)hydroxides, such as electrocatalytic activity of transition-metal oxy-hydroxides in the oxygen evolution reaction (OER) and ion exchange capabilities of layered double hydroxides (LDHs), continue to attract significant interest. However, these compounds are typically synthesized in aqueous solutions at room temperature, under hydrothermal conditions, or in mild vapor atmospheres. Here, we present a novel (oxy-)hydroxide synthesis technique called "vapor hydroxidation," which is conducted in a highly concentrated water vapor atmosphere at elevated temperatures. Structural analysis revealed the formation of a new oxy-hydroxide, $[Ba_2O_x(OH)_y]_{0.55}InO_2$, with a misfit-layered structure, characterized by alternating incommensurate barium hydroxide bilayers and indium oxide blocks. Unlike known (oxy-)hydroxides, this oxy-hydroxide displays exceptional thermal stability, retaining hydroxide ions within its crystal structure up to approximately 700 °C. These features suggest promising potential for high-temperature proton conductivity, as demonstrated by an electrical conductivity of 5×10^{-4} S cm^{-1} at 500 °C even under dry argon. Our "vapor hydroxidation" method thus opens up a new avenue for the development of proton-functional materials with unconventional chemical and electronic characteristics.

Received 22nd February 2025
Accepted 15th May 2025

DOI: 10.1039/d5ta01492a

rsc.li/materials-a

Open Access Article. Published on 28 May 2025. Downloaded on 2/16/2026 5:53:43 AM.
This article is licensed under a Creative Commons Attribution 3.0 Unported Licence.

Introduction

The functionalities associated with protons (H^+) are crucial across numerous research areas,[1,2] including catalytic,[3,4] biological,[5] and electrochemical processes,[6] where proton-incorporating inorganic solids play significant roles. For instance, zirconium- and cerium-based perovskite oxides, such as $BaCe_{0.9}Y_{0.1}O_{3-\delta}$ and $BaZr_{0.9}Y_{0.1}O_{3-\delta}$, exhibit high proton conductivity when incorporating hydroxide ions in humid atmospheres, and are used in solid oxide fuel cells (SOFCs) and water electrolyzers.[7] Unlike proton-conducting polymers exhibiting thermal instability,[8] these materials demonstrate excellent stability and long-term durability at elevated temperatures, typically above 400 °C. However, such oxide-based proton carriers require external proton sources, thereby restricting the operation conditions of these devices.

Hydroxides and oxy-hydroxides represent potential high-density proton carriers owing to their hydroxide-rich compositions. Recent advancements in (oxy-)hydroxides have highlighted their importance as materials for energy and environmental applications. In particular, layered double hydroxides (LDHs) benefit from their unique structural properties, where proton incorporation enhances chemical reactions and ion exchange capabilities, making them valuable as catalysts, adsorbents, and battery materials. However, their use at elevated temperatures has been limited by thermal instability, which leads to phase decomposition into oxides and water molecules. This instability complicates the retention of protons within the crystal structure above the decomposition temperature, as it requires maintaining high water vapor pressures. Accordingly, developing novel (oxy-)hydroxides with improved thermal stability is essential for advancing proton-related functionalities.

Traditionally, hydroxides and oxy-hydroxides have been synthesized under mild aqueous conditions, often through precipitation[9–11] or hydrothermal methods.[12,13] These techniques effectively produce phases with controlled morphologies,[14] particle sizes,[15] and crystal structures.[16] For example,

[a]Department of Applied Chemistry, Faculty of Chemistry and Biochemistry, Kanagawa University, 3-27-1 Rokkakubashi, Kanagawa-ku, Yokohama, 221-8686, Japan. E-mail: t-mot@kanagawa-u.ac.jp
[b]Skoltech Center for Energy Science and Technology, Skolkovo Institute of Science and Technology, 121205 Moscow, Russia
[c]Advanced Imaging Core Facility, Skolkovo Institute of Science and Technology, 121205 Moscow, Russia
[d]Department of Chemistry, Kindai University, Osaka 577-8502, Japan
[e]Department of Energy and Hydrocarbon Chemistry, Graduate School of Engineering, Kyoto University, Kyoto, 615-8510, Japan

† Electronic supplementary information (ESI) available. See DOI: https://doi.org/10.1039/d5ta01492a

This journal is © The Royal Society of Chemistry 2025

Open Access Article. Published on 28 May 2025. Downloaded on 2/16/2026 5:53:43 AM.
This article is licensed under a Creative Commons Attribution 3.0 Unported Licence.

hydrothermal methods have been employed to synthesize complex oxy-hydroxides, such as $Cu_3V_2O_7(OH)_2$ (ref. 17) and $Ag_2Cu_3Cr_2O_8(OH)_4$,[18] at temperatures around 100 °C. Recently, alternative approaches, including solvothermal and mechanochemical processes, have been explored to achieve greater control over phase composition and to synthesize metastable phases.[19] Moreover, some oxy-hydroxides can be formed through gas-phase reactions between oxides and water vapor. Brownmillerite-type $Ba_2In_2O_5$, which contains a large number of oxygen vacancies, transforms into a perovskite-type $Ba_2In_2O_4(OH)_2$ with a tetragonal structure (denoted as "t-BI") when annealed at approximately 300 °C under flowing N_2 gas saturated with water vapor at room temperature.[20–22] The Steam-Hydrothermal Treatment (SHT) method utilizes high-pressure steam at temperatures typically ranging from 100 °C to 350 °C to create nanostructures on oxide and metal surfaces, enhancing biocompatibility and functionality.[23] In addition, combining Micro-Arc Oxidation (MAO) with SHT enables hydroxyapatite (HA) coating on titanium (Ti) surfaces, promoting bone formation (osseointegration).[24]

This study investigated the synthesis of (oxy-)hydroxides under previously unexplored conditions,[25] utilizing high temperatures in concentrated water vapor. Starting from barium–indium oxides as precursors, a heat treatment at 500 °C under 80 vol% water vapor led to the discovery of a new oxy-hydroxide with a misfit-layered structure. Importantly, the reaction temperature of 500 °C exceeds the dehydration (decomposition) temperatures of most hydroxides and oxy-hydroxides, conditions that are typically avoided except in the context of water vapor-assisted sintering for several oxides.[26–28] This unique reaction environment (see the summary of synthesis methods in Table S1 of the ESI†) enables the synthesis of such a novel material. We present the synthesis and crystal structure of this oxy-hydroxide, along with its proton conductive properties. Our synthesis method, termed "vapor hydroxidation," marks significant advancements in the development of proton-related functional materials with unconventional chemical and electronic characteristics.

Results and discussion

Compositional and structural determination

As presented in Fig. 1, when the $Ba_2In_2O_5$ precursor reacts with 80 vol% water vapor at 200 °C for three hours, a known tetragonal phase of $Ba_2In_2O_4(OH)_2$ with a perovskite structure ("t-BI") is formed. Previous research indicated that the formation of t-BI requires prolonged heat treatment, typically lasting several days, when heating $Ba_2In_2O_5$ at 200 °C under moist air containing less than 2.5 vol% water vapor.[20–22] This study demonstrates that highly concentrated water vapor significantly accelerates phase formation, allowing the rapid synthesis of t-BI within three hours. In contrast, the product treated under 80 vol% water vapor at 500 °C exhibits unprecedented diffraction peaks, along with minor impurity peaks from In_2O_3. Specifically, a series of reflections at $2\theta = 9.04°$, 18.20°, 27.84°, and 56.90° (corresponding to $d = 9.77$ Å, 4.87 Å, 3.20 Å, and 1.62 Å, respectively) suggests that the newly synthesized compound,

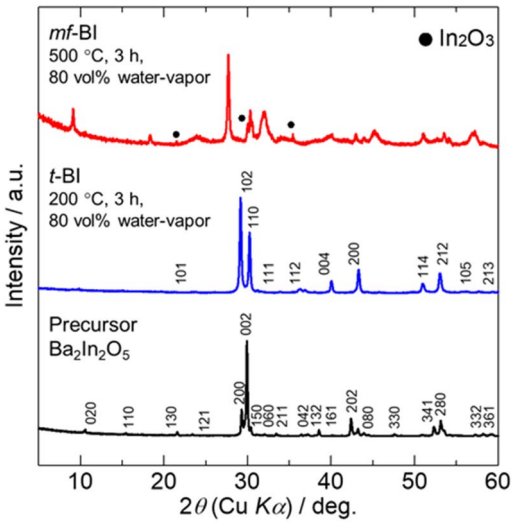

Fig. 1 X-ray powder diffraction patterns for the $Ba_2In_2O_5$ precursor and its derivatives synthesized under highly concentrated water vapor: the products synthesized at 500 °C (upper) and at 200 °C (middle) for 3 hours under 80 vol% water vapor.

possibly a Ba–In oxy-hydroxide, crystallizes in a layered structure. Notably, attempts at conventional hydrothermal/solvothermal syntheses of Ba–In oxy-hydroxides always ended in the formation of known indium hydroxide or barium compounds as the primary phases, as detailed in the section of the ESI† "Comparative sample syntheses by hydrothermal/solvothermal methods" and demonstrated in Table S2 and Fig. S1.†

The selected area electron diffraction (SAED) pattern along the [001] direction (Fig. 2a) is characteristic of a composite incommensurately modulated structure, consisting of two subsystems with periodicities of $b_1 = 3.2$ Å and $b_2 = 5.9$ Å along the *b*-axis, while sharing a common periodicity along the *a*-axis ($a = 5.6$ Å). On the other hand, the [$\bar{1}$10] SAED pattern (Fig. 2b) displays a longer periodicity of 9.8 Å along the *c*-axis, consistent with the XRD observation shown above. High-angle annular dark-field scanning transmission electron microscopy (HAADF-

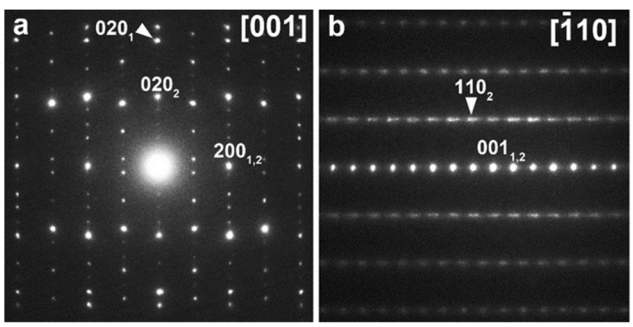

Fig. 2 SAED patterns for the Ba–In oxy-hydroxide (mf-BI). (a) [001] SAED pattern showing the incommensurate composite structure, with subscripts 1 and 2 indicating diffraction spots from the first and second subsystems, respectively. (b) [$\bar{1}$10] SAED pattern along the second subsystem.

Open Access Article. Published on 28 May 2025. Downloaded on 2/16/2026 5:53:43 AM. This article is licensed under a Creative Commons Attribution 3.0 Unported Licence.

STEM) further unveils the alternate stacking of single In and double Ba layers along the *c*-axis (Fig. S2†), offering a clearer view of the layered structure.

The electron diffraction pattern, involving two distinct periodicities along the *b*-axis, resembles those observed in a misfit-layered cobalt oxide of $[Ca_2CoO_3]_{0.62}CoO_2$ with a composite modulated monoclinic structure.[29,30] These misfit-layered compounds follow the general formula $[M_mA_2X_{m+2}]_qBX_2$, characterized by alternating layers of hexagonal (BX_2) and rock-salt ($M_mA_2X_{m+2}$) blocks. In this formula, M stands for a heavy or transition metal, *m* denotes the number of MX layers, A refers to an alkaline earth metal, and X can be S, Se, O, or OH. Such structures form composite crystals with dual *b*-axis lengths, leading to an irrational misfit ratio ($q = b_1/b_2$). It is noteworthy that misfit-layered Ca–Co and Sr–Co oxy-hydroxides, which incorporate hydroxide ions into their rock-salt layers, have also been identified previously.[31,32] This resemblance suggests that the Ba–In oxy-hydroxide adopts a similar misfit-layered structure, referred to hereafter as "mf-BI." In mf-BI, the BO_2 block contains InO_2, while the rock-salt block comprises double Ba(O,OH), yielding a chemical formula of $[Ba_2(O,OH)_2]_qInO_2$. The misfit ratio for mf-BI, estimated as $q \approx 0.55$ from SAED, agrees closely with the range of 0.55 to 0.58 observed for the Sr- and Ca-based cobalt oxy-hydroxides but is slightly larger than 0.50 reported for Ba-based cobalt oxides.[29–34]

Energy-dispersive X-ray spectroscopy (EDX) analysis (Fig. S3†) shows a homogeneous distribution of indium and barium with an atomic ratio of Ba : In = 1.12(3) : 1.00(3). This composition suggests a slight excess of barium and a deficiency of indium compared to the nominal Ba/In ratio of 1.0, consistent with the presence of an In_2O_3 impurity observed in the sample. To improve the phase purity of mf-BI, a series of samples with varying Ba/In ratios were synthesized. As seen in Fig. S4,† the level of In_2O_3 impurity decreases as the nominal Ba/In ratio increases from 1.00 to 1.10. Based on these observations, a Ba/In ratio of 1.10 is determined to be the optimal cationic composition for mf-BI, corroborating the *q* value in its chemical formula.

Fourier transform infrared spectroscopy (FT-IR) reveals that both t-BI and mf-BI samples exhibit IR bands associated with O–H stretching vibrations in the frequency range of 2700 cm^{-1} to 3700 cm^{-1} (Fig. 3a). t-BI shows two broad bands at 2900 cm^{-1} and 3650 cm^{-1}, which have been previously linked to distinct proton positions.[35,36] In contrast, mf-BI presents a unique spectral shape, where the overlap of narrow and broad components suggests a more complex bonding nature of hydroxide ions. Importantly, at 400 °C, mf-BI exhibits significant spectral changes compared to room temperature (Fig. 3b), with peak broadening at 3300 cm^{-1} and the disappearance of peaks at 3450 cm^{-1} and 3550 cm^{-1}, emphasizing proton migration within the crystal structure. A more detailed discussion of the FT-IR spectra is provided in the ESI.†

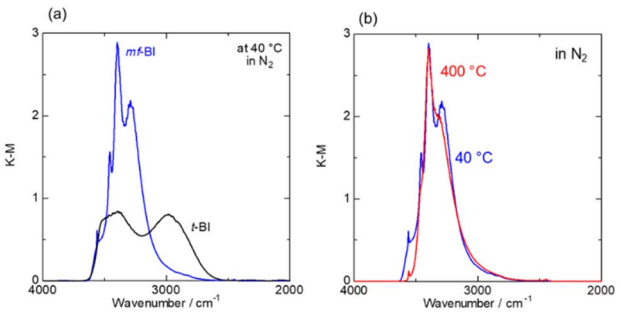

Fig. 3 FT-IR spectra of (a) t-BI (black) and mf-BI (blue) at 40 °C and (b) mf-BI at 40 °C (blue) and 400 °C (red) under flowing N_2 gas.

The discovery of the new oxy-hydroxide, mf-BI, represents several significant advances in materials science. The synthesis at high temperatures in concentrated water vapor—a method we have termed "vapor hydroxidation"—opens up a new avenue for exploring innovative (oxy-)hydroxide materials. Our "vapor hydroxidation" method highlights the advantages of using concentrated water vapor for synthesizing (oxy-)hydroxides. While the hydrothermal method is generally recognized for its effectiveness due to the high reactivity of liquid water,[37,38] increased reaction temperatures can often cause instability of reactants and products in solution. In contrast to hydrothermal synthesis, "vapor hydroxidation" does not rely on liquid water; instead, it involves a reaction between the solid and gas phases to enable the high-temperature formation of (oxy-)hydroxides. This distinction is crucial as it allows the method to be applied to solid materials that may dissolve or degrade upon contact with liquid water.

Although heat treatments in concentrated water vapor—commonly referred to as "Steam-Hydrothermal Treatment (SHT)"—have been previously investigated, these studies mainly focused on surface modifications of oxides and metals. Supercritical hydrothermal reactions conducted above the critical point of water (374 °C, 22.1 MPa) typically yield oxides.[39,40] Distinct from these approaches, our "vapor hydroxidation" method promotes the formation of novel oxy-hydroxides as stable phases. This is achieved under previously unexplored thermodynamic equilibrium conditions. The sufficiently high water vapor pressures, which are an order of magnitude higher than those in conventional humid atmospheres, are suggested to stabilize (oxy-)hydroxides even at elevated temperatures.

Our new synthesis method has consequently produced a compound possessing unique electronic properties. mf-BI represents the first example of an electrical insulator among misfit-layered compounds. Unlike all previously reported electrically conductive misfit-layered oxides,[29] sulfides,[41,42] and oxy-hydroxides,[43] mf-BI is free from transition metals and is characterized by its white color, indicative of its insulating properties. Further, as detailed later, our impedance measurements reveal that mf-BI exhibits dominant proton conduction, highlighting its potential as a proton conductor.

Thermal behaviors

As indicated by thermogravimetry (TG) in Fig. 4, t-BI exhibits a significant weight loss at approximately 300 °C in a dry N_2 atmosphere, whereas mf-BI displays three distinct weight loss steps at approximately 200 °C, 500 °C, and 750 °C. Mass

 This journal is © The Royal Society of Chemistry 2025

Open Access Article. Published on 28 May 2025. Downloaded on 2/16/2026 5:53:43 AM.
This article is licensed under a Creative Commons Attribution 3.0 Unported Licence.

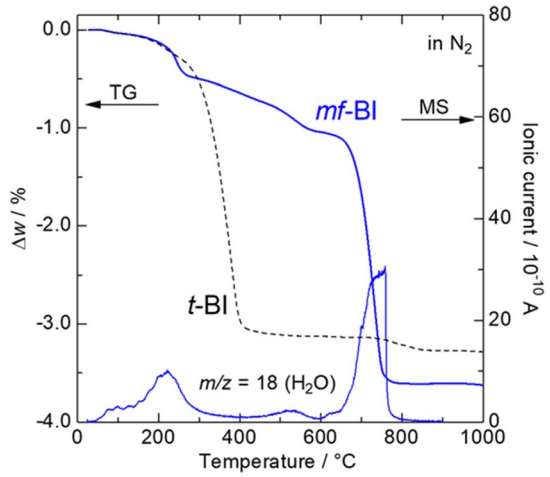

Fig. 4 TG curves of mf-BI (blue) and t-BI (black dash) upon heating in flowing N_2 gas, with corresponding MS data for $m/z = 18$ (water desorption).

spectroscopic (MS) analysis identifies water desorption ($m/z = 18$) at each step. The initial minor weight loss at 200 °C is attributed to the desorption of surface water species. Remarkably, mf-BI retains a substantial amount of hydroxide ions exceeding 700 °C, with primary water desorption occurring thereafter, leading to structural collapse. Indeed, the mf-BI sample reverts to poorly crystalline $Ba_2In_2O_5$ when heat-treated at 1000 °C under flowing N_2 gas (Fig. S5†). Additionally, a minor weight loss step associated with water desorption is also observed at 500 °C.

It is well recognized that hydroxides and oxy-hydroxides, including layered double hydroxides (LDH),[44,45] t-BI, and $Ba(Zr,Y)O_{3-\delta-y}(OH)_{2y}$,[46] tend to desorb hydroxide ions (undergo dehydration) at much lower temperatures, typically between 200 °C and 400 °C, in a dry atmosphere. Thus, the unusually high water desorption temperature of mf-BI is surprising and suggests potential applications in previously unexplored practical fields. The significant thermal stability of mf-BI likely originates from the robust framework of the Ba hydroxide block, which comprises strong chemical bonds between Ba cations and OH^- anions. The presence of strong Ba–OH bonds is consistent with the high water desorption temperature of $Ba(OH)_2$, as demonstrated by the TG data in Fig. S6.† Moreover, the unconventional O–H bonding nature of mf-BI, as revealed by the FT-IR spectra, indicates that its unique local environment surrounding the hydroxide ions could play an additional role in this behavior.

High-temperature synchrotron X-ray powder diffraction (HT-SXRD) reveals no substantial changes up to 300 °C (Fig. 5). However, beyond 400 °C, distinct changes in positions and intensities of the diffraction peaks are observed, particularly between $2\theta = 7.0°$ and 8.5°. This observation coincides with the second weight loss observed in the TG curve, suggesting that the changes in the diffraction pattern are due to a structural transformation associated with hydroxide ion desorption. In

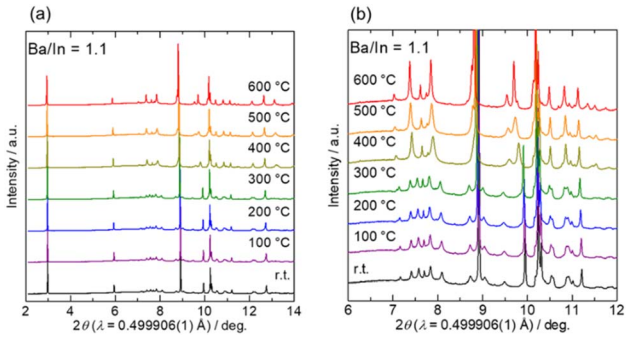

Fig. 5 HT-SXRD patterns for mf-BI upon heating in an N_2 atmosphere. (a) Patterns at 2° to 14°; (b) at 6° to 12° 2θ range, observed with a wavelength of 0.499906(1) Å.

fact, this transformation is irreversible in a dry atmosphere, and the sample does not revert to the LT phase upon cooling.

Le Bail fitting using an approach of (3 + 1)-dimensional crystallography distinguishes between the crystalline phases at room temperature (LT phase) and 600 °C (HT phase). The HT phase, characterized by a misfit-layered structure with monoclinic symmetry, is well-fitted using the (3 + 1)-dimensional superspace group $X2/m(0\beta0)s0$, where $X = [1/2, 1/2, 0, 1/2]$. The lattice parameters are: $a = 5.6791(1)$ Å, $b_1 = 3.22887(8)$ Å, $c = 9.8410(2)$ Å, $\beta = 96.943(2)°$, $q = 0.54569(3)b_1^*$ ($b_2 = 5.9170$ Å). Detailed Rietveld refinement for the HT phase is provided in the ESI.† Our structural study indicates that the crystal structure of mf-BI is similar to $(CaOH)_{1.15}CoO_2$.[47] In our structure model, the InO_2 block possesses a pseudo-triangular arrangement of In atoms that are octahedrally coordinated by oxygen, forming edge-shared InO_6 octahedra. Meanwhile, the $Ba_2(O,OH)_2$ block adopts a highly distorted rock-salt structure, as schematically shown in Fig. 6. Maintaining charge neutrality with the formal oxidation states of Ba^{2+} and In^{3+}, and given that these cations fully occupy their respective sites, the estimated composition is $[Ba_2O_{0.168}(OH)_{1.832}]_{0.546}InO_2$.

The LT phase exhibits pronounced reflection splitting, indicating a symmetry lowering from monoclinic to triclinic. The room temperature diffraction pattern can be indexed using two *C*-centered triclinic unit cells, yielding the following lattice parameters: $a = 5.6812(6)$ Å, $b = 3.2180(2)$ Å, $c = 9.770(1)$ Å, $\alpha = 89.408(9)°$, $\beta = 96.947(2)°$, $\gamma = 90.033(8)°$ for the subsystem I (InO_2 block) and $a = 5.6596(2)$ Å, $b = 5.7983(3)$ Å, $c = 9.7722(4)$

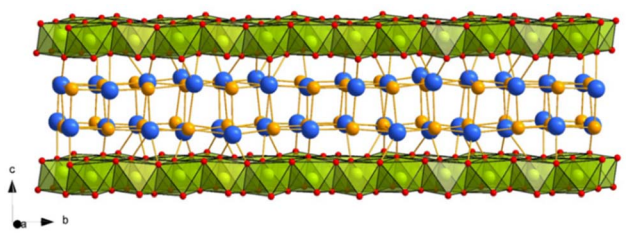

Fig. 6 The mf-BI crystal structure at 600 °C shown as a commensurate approximant with $b = 11b_1$. The In, O, Ba atoms, and OH groups are depicted in green, red, blue, and orange, respectively.

Open Access Article. Published on 28 May 2025. Downloaded on 2/16/2026 5:53:43 AM. This article is licensed under a Creative Commons Attribution 3.0 Unported Licence.

Å, $\alpha = 92.919(6)°$, $\beta = 96.947(2)°$, $\gamma = 90.072(3)°$ for the subsystem II ($Ba_2(O,OH)_2$ block). However, severe reflection overlap and anisotropic peak broadening in both subsystems prevent Rietveld refinement for this triclinic misfit-layered structure. Assuming the charge neutrality and a fixed cationic ratio at Ba/In = 1.091, the composition of the LT phase can be expressed as $[Ba_{1.958}O_{0.120}(OH)_{1.880}]_{0.558}InO_2$. The formula weights of 315.60 for the LT phase and 315.17 for the HT phase indicate that the LT-to-HT phase transformation involves weight loss due to hydroxide ion desorption, consistent with the TG data, although the observed weight loss slightly exceeds the calculated value.

Electrical conductivity

In conventional oxide-based proton conductors, oxygen vacancy sites react with externally supplied water molecules, which serve as proton sources. These protons act as charge carriers, resulting in the emergence of electrical conductivity. A key finding of this study is that proton conduction in mf-BI occurs even without the need for an external proton source.

The electrical conductivity of mf-BI was measured using the AC impedance method to investigate the possibility of proton conduction. The conductivity data of a reference sample of $(ZrO_2)_{0.92}(Y_2O_3)_{0.08}$ (8YSZ), measured using our experimental setup, are presented in Fig. S7† and show good agreement with previously reported values in the literature.[48] Nyquist plots, obtained during both heating and cooling under a dry Ar atmosphere, show distorted semicircles (Fig. S8†), which are well-fitted with an equivalent circuit depicted in the inset. The Arrhenius plot of bulk conductivity (Fig. 7) reveals a noticeable change in slope around 400 °C upon heating, accompanied by a sharp increase in conductivity to approximately 10^{-4} S cm^{-1} at 500 °C. During cooling, the conductivity decreases exponentially, with an activation energy of 0.96 eV, and the hysteresis is likely due to the aforementioned structural transformation observed upon heating. A careful examination of the deuterium-substitution effect suggests that mf-BI functions as a proton conductor even in a dry atmosphere, as detailed in the ESI (Fig. S9–S12†). Further, these observations reveal that the HT phase is more electrically conductive than the LT phase.

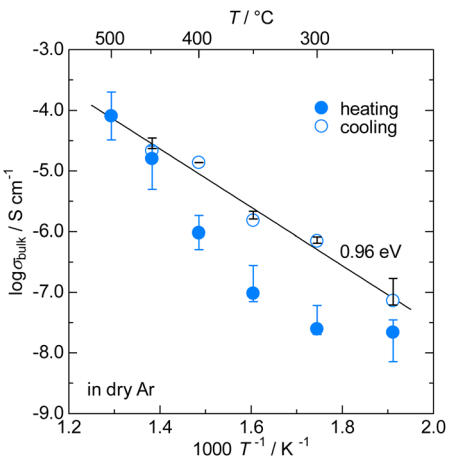

Fig. 7 Arrhenius plots of bulk electrical conductivity of mf-BI upon heating and cooling in a dry Ar atmosphere. Error bars in the figure represent the standard deviation of the data obtained from multiple measurements (six data points during heating and three during cooling).

The $\sigma_{bulk}T$ *vs.* $P(O_2)$ plot at 500 °C (Fig. S13†) shows that electrical conductivity remains constant in the range $-18 \leq \log P(O_2)/\text{atm} \leq -4$, indicating predominant proton conduction with minimal electronic contributions. At both lower ($-19 \leq \log P(O_2)/\text{atm} \leq -28$) and higher ($-2 \leq \log P(O_2)/\text{atm} \leq 0$) oxygen partial pressures, the conductivity increases. The enhanced conductivity at low oxygen partial pressures likely originates from n-type conduction due to material reduction, as observed in indium oxides. The increase at high oxygen partial pressures is less clear but may be related to p-type conduction from BaO peroxidation in the $Ba_2(O,OH)_2$ block.

Let us examine the proton conduction mechanism in mf-BI. The crystal structure of mf-BI, with its alternate InO_2 and $Ba_2(O,OH)_2$ blocks, suggests two potential proton conduction pathways along the *ab* plane. The first pathway involves proton migration within the $Ba_2(O,OH)_2$ block, while the second involves proton migration between the InO_2 and $Ba_2(O,OH)_2$ blocks. Elucidating the detailed proton migration kinetics requires a comprehensive analysis combining analytical techniques such as ^{1}H nuclear magnetic resonance and neutron diffraction with first-principles calculations. However, it should be noted that such investigations are inherently challenging due to the highly complex crystallographic nature of mf-BI, which complicates the precise interpretation of both experimental and theoretical data. To the best of our knowledge, no theoretical studies have yet explored the relationship between proton conductivity and the crystal structure of misfit-layered (oxy-)hydroxides.

The enhanced electrical conductivity of mf-BI, observed upon heating above 400 °C and during the subsequent cooling process, can be reasonably linked to its thermal behavior. The TG analysis reveals that the transition from the LT to HT phase involves partial desorption of hydroxide ions. In the LT phase, the higher occupancy of hydroxide ions in the $Ba_2(O,OH)_2$ block would reduce the availability of proton hopping sites. In contrast, the HT phase, with fewer hydroxide ions (*i.e.*, a larger number of hydroxide deficiencies), facilitates more frequent proton hopping, resulting in increased proton conductivity. Interestingly, unlike conventional proton conductors,[49,50] mf-BI exhibits a slight decrease in electrical conductivity under a humid Ar atmosphere (Fig. 8), which supports our hypothesis. This behavior, which is analogous to hole doping in electrical insulators, suggests that anionic defect formation is an effective strategy for enhancing proton conductivity in hydroxides.

Traditional research on proton conductors has largely focused on perovskite-related and pyrochlore-type oxides, such as chemically substituted $BaMO_3$ (M = Zr, Ce)[51–54] and $La_2Zr_2O_7$.[55,56] More recently, Yashima and coworkers have reported hexagonal perovskite-related oxides $Ba_5Er_2Al_2ZrO_{13}$ (ref. 57) and β-Ba_2ScAlO_5.[58] However, known materials typically require external proton sources, and the exploration of novel proton conductors beyond these traditional oxide types remains

 This journal is © The Royal Society of Chemistry 2025

Open Access Article. Published on 28 May 2025. Downloaded on 2/16/2026 5:53:43 AM.
This article is licensed under a Creative Commons Attribution 3.0 Unported Licence.

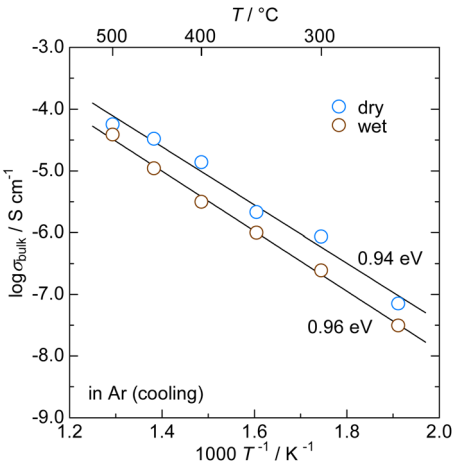

Fig. 8 Arrhenius plots of bulk electrical conductivity. The blue and brown circles denote data plots measured upon cooling in dry and wet Ar atmospheres, respectively.

limited. In contrast, this study presents a new strategy for synthesizing (oxy-)hydroxides with efficient proton conductivity even in a dry atmosphere (see the list of representative proton conductors in Table S3†). The development of such oxy-hydroxides establishes new design guidelines for advancing superior proton conductors.

Conclusions

We have developed a new synthesis method of (oxy-)hydroxides, which involves high-temperature heat treatment in highly concentrated water vapor, enabling the formation of a barium–indium oxy-hydroxide, $[Ba_2O_x(OH)_y]_{0.55}InO_2$. Structural analysis, including transmission electron microscopy and synchrotron X-ray diffraction, revealed that the newly synthesized oxy-hydroxide has a misfit-layered structure with alternating barium hydroxide double layers and indium oxide blocks arranged in an incommensurate manner. Remarkably, the oxy-hydroxide ("mf-BI") exhibits exceptionally high thermal stability, with hydroxide ions remaining intact up to approximately 700 °C. In addition, mf-BI functions as a proton conductor at temperatures up to 500 °C, even in dry atmospheres, in contrast to conventional oxide-based proton conductors that require external proton sources. This novel synthesis method and the resulting oxy-hydroxide represent a considerable advancement in the search for new proton-conducting materials and other functional applications, such as acid-catalyzed reactions at elevated temperatures. In addition, the unique crystallographic features inherent in misfit-layered structures may induce unconventional dielectric and optical properties.

Experimental

Samples of Ba–In oxy-hydroxides were synthesized *via* the citrate-lactate route. $BaCO_3$ (99.99%, FUJIFILM Wako Pure Chemical) and In_2O_3 (99.99%, Kojundo Chemical Laboratory) served as the starting materials. Appropriate amounts of these reagents were dissolved in aqueous solutions of citric and lactic acids (for $BaCO_3$) or nitric acid (for In_2O_3), with the citric and lactic acids present in a threefold molar excess. These solutions were mixed in an alumina crucible and heated at 120 °C to promote polymerization. The resultant gelatinous product was calcined in air stepwise at 450 °C for 1 hour, 600 °C for 1 hour, and 1000 °C for 10 hours. The calcined powder was further fired in the air at 1200 °C for 10 hours to prepare an oxide precursor. This precursor was pressed into pellets at 5 MPa and heat-treated in a highly concentrated water vapor atmosphere at 200 °C or 500 °C for 3 hours using a reactor, as schematically depicted in Fig. S14.† Approximately 80 vol% water vapor was generated by directly injecting 64 μL min^{-1} of liquid water into the vertical tube furnace with a 20 mL min^{-1} N_2 gas. The partial pressure of water vapor can be estimated based on a simple calculation using the ideal gas volume of the injected liquid water relative to the balanced N_2 gas flow in the reactor open to the atmosphere.

Phase purity and lattice parameters of the products were analyzed using X-ray powder diffraction (XRD, Ultima IV Protectus; Cu Kα radiation, Rigaku). The measurements were performed at room temperature in an angular range from 10° to 90° with a step size of 0.02°. Additionally, high-temperature synchrotron X-ray diffraction analysis (HT-SXRD) was conducted at BL02B2 in SPring-8 using a one-dimensional solid-state detector (MYTHEN, DECTRIS[59]). The X-ray wavelength was $\lambda = 0.499906(1)$ Å. For this analysis, the powder sample was placed in a quartz capillary (0.2 mm in diameter), and diffraction data were collected up to 800 °C using a temperature program detailed in Fig. S15.† Le Bail and Rietveld refinements of laboratory-XRD and HT-SXRD patterns were done using Jana2006 software.[60]

Crystallographic features of the Ba–In oxy-hydroxide (mf-BI) were investigated by transmission electron microscopy (TEM). The TEM sample was prepared by grinding the crystals in a mortar with ethanol and depositing drops of the suspension onto a holey carbon grid. Selected area electron diffraction (SAED) patterns, high-angle annular dark field scanning transmission electron microscopy (HAADF-STEM) images, and energy-dispersive X-ray (EDX) maps were observed using an aberration-corrected FEI Titan G3 electron microscope equipped with a Super-X EDX system and operated at 200 kV.

Fourier transform infrared spectroscopy (FT-IR) measurements were conducted employing a diffuse reflection method with an FT-IR spectrometer (FT/IR-4700, JASCO) equipped with an *in situ* measurement chamber (DR-650Ai, JASCO). A DLATGS detector and a CaF_2 optical window were used for the measurements. The background spectrum was obtained from commercial KBr (infrared spectrophotometry grade, FUJIFILM Wako Pure Chemical). The analysis covered a wavenumber range from 1000 cm^{-1} to 4000 cm^{-1} at temperatures ranging from 40 °C to 600 °C in a dry N_2 gas atmosphere (150 mL min^{-1}). Spectral Manager Software (JASCO) was employed for baseline corrections, establishing a straight line between 2000 cm^{-1} and 4000 cm^{-1}, and removing signals attributed to

Open Access Article. Published on 28 May 2025. Downloaded on 2/16/2026 5:53:43 AM. This article is licensed under a Creative Commons Attribution 3.0 Unported Licence.

H_2O and CO_2. Additionally, the spectra were converted to Kubelka–Munk units (K–M) using the Kubelka–Munk function.

Thermal behaviors of mf-BI were investigated using a thermogravimetric-differential thermal analyzer (TG-DTA; Thermo Plus Evo2 TG-DTA8122, Rigaku) in a flowing N_2 gas (50 mL min^{-1}) with a heating profile to 1000 °C at a scan rate of 10 °C min^{-1}. Desorbed gas species were analyzed by a quadrupole mass spectrometer (Q-MS; Transpector CPM, INFICON) in a flowing N_2 gas (10 mL min^{-1}) at a heating rate of 10 °C min^{-1}.

For electrical conductivity measurements, the mf-BI powder was pressed into pellets under a uniaxial pressure of approximately 5 MPa followed by cold isostatic pressing at 250 MPa. The pellets were sintered in 80 vol% water vapor at 500 °C for 20 hours. The relative density of the sintered pellets typically ranged from 78.5% to 80.5%. A Pt paste (TR-7907, Tanaka Precious Metals) was applied to the surface of the sample and heat-treated in 80 vol% water vapor at 500 °C for 3 hours. The bulk conductivity of the mf-BI pellets was measured using an AC analyzer (SP-300, BioLogic) with an applied voltage of 30 mV and a measurement frequency ranging from 7 MHz to 1 Hz. The measurements were conducted in a dry Ar atmosphere at 50 °C intervals within a temperature range between 200 °C and 500 °C. The dew point of the outlet Ar gas of the measurement cell was monitored using a direct mirror-cooled dew point sensor (D-2-SR, General Eastern) and a dew point monitor (OptiSonde, General Eastern) to ensure the water vapor partial pressure remained nearly constant below 0.25 hPa. Measurements in wet Ar gas (under a saturated water vapor pressure at room temperature, 30.6 hPa) were performed for a selected sample. The dependence of electrical conductivity on the oxygen partial pressure $P(O_2)$ was also measured in a dry atmosphere over the range of $-28 \leq \log P(O_2)$ (atm) ≤ 0, using a PID oxygen partial pressure controller (SiOC-200CB, STLab) with Ar, O_2, and Ar/O_2 mixture.

Data availability

The data supporting this article have been included as part of the ESI.†

Author contributions

K. A., Y. K., Y. A., S. O., M. K., I. S., and F. T. conducted the experiments and analyzed the data. K. A. and M. S. wrote the original draft, and T. M. reviewed and edited the manuscript based on the suggestions and comments from A. A. and H. K. All authors approved the final version of the manuscript. M. S., H. K., and T. M. secured funding. T. M. managed the project administration.

Conflicts of interest

There are no conflicts to declare.

Acknowledgements

This work was partly supported by Grant-in-Aid for Scientific Research on Innovative Areas “Mixed anion” (JP16H06440, JP17H05490, and JP19H04707), Grant-in-Aid for Transformative Research Areas (A) “Supra-ceramics” (JP22H05143), Grant-in-Aid for Specially Promoted Research (JP22H04914), and Grant-in-Aid for Scientific Research (C) (JP18K04713, JP25K08282) from the Japan Society for the Promotion of Science (JSPS). The synchrotron radiation experiments were conducted at BL02B2 in SPring-8 with the approval of the Japan Synchrotron Radiation Research Institute (JASRI) (Proposal No. 2019B1776).

References

1 A. Y. Mulkidjanian, J. Heberle and D. A. Cherepanov, *Biochim. Biophys. Acta, Bioenerg.*, 2006, **1757**, 913–930.
2 S. Hammes-Schiffer, *J. Am. Chem. Soc.*, 2015, **137**, 8860–8871.
3 Y. He, S. Liu, C. Priest, Q. Shi and G. Wu, *Chem. Soc. Rev.*, 2020, **49**, 3484–3524.
4 Y. Watanabe, K. Hyeon-Deuk, T. Yamamoto, M. Yabuuchi, O. M. Karakulina, Y. Noda, T. Kurihara, I.-Y. Chang, M. Higashi, O. Tomita, C. Tassel, D. Kato, J. Xia, T. Goto, C. M. Brown, Y. Shimoyama, N. Ogiwara, J. Hadermann, A. M. Abakumov, S. Uchida, R. Abe and H. Kageyama, *Sci. Adv.*, 2022, **8**, eabm5379.
5 G. A. Voth, *Acc. Chem. Res.*, 2006, **39**, 143–150.
6 S. Choi, T. C. Davenport and S. M. Haile, *Energy Environ. Sci.*, 2019, **12**, 206–215.
7 M. Chen, X. Xie, J. Guo, D. Chen and Q. Xu, *J. Mater. Chem. A*, 2020, **8**, 12566–12575.
8 S. Bureekaew, S. Horike, M. Higuchi, M. Mizuno, T. Kawamura, D. Tanaka, N. Yanai and S. Kitagawa, *Nat. Mater.*, 2009, **8**, 831–836.
9 F. Cavani, F. Trifirb and A. Vaccari, *Catal. Today*, 1991, **11**, 173–301.
10 F. L. Theiss, G. A. Ayoko and R. L. Frost, *Appl. Surf. Sci.*, 2016, **383**, 200–213.
11 M. V. Bukhtiyarova, *J. Solid State Chem.*, 2019, **269**, 494–506.
12 D. P. Singh, A. K. Ojha and O. N. Srivastava, *J. Phys. Chem. C*, 2009, **113**, 3409–3418.
13 M. Mohapatra and S. Anand, *Int. J. Eng. Sci. Technol.*, 2010, **2**, 127–146.
14 J. Lv, L. Qiu and B. Qu, *J. Cryst. Growth*, 2004, **267**, 676–684.
15 Y. Ding, G. Zhang, H. Wu, B. Hai, L. Wang and Y. Qian, *Chem. Mater.*, 2001, **13**, 435–440.
16 Z. Liu, R. Ma, M. Osada, K. Takada and T. Sasaki, *J. Am. Chem. Soc.*, 2005, **127**, 13869–13874.
17 X. Sun, J. Wang, Y. Xing, Y. Zhao, X. Liu, B. Liu and S. Hou, *CrystEngComm*, 2011, **13**, 367–370.
18 N. Casan-Pastor, J. Rius, O. Vallcorba, I. Peral, J. Oró-Solé, D. S. Cook, R. I. Walton, A. García and D. Muñoz-Rojas, *Dalton Trans.*, 2017, **46**, 1093–1104.
19 C. Prasad, H. Tang, Q. Q. Liu, S. Zulfiqar, S. Shah and I. Bahadur, *J. Mol. Liq.*, 2019, **289**, 111114.

 This journal is © The Royal Society of Chemistry 2025

Open Access Article. Published on 28 May 2025. Downloaded on 2/16/2026 5:53:43 AM. This article is licensed under a Creative Commons Attribution 3.0 Unported Licence.

20 J. Bielecki, S. F. Parker, D. Ekanayake, S. M. H. Rahman, L. Börjesson and M. Karlsson, *J. Mater. Chem. A*, 2014, **2**, 16915–16924.
21 T. Schober and J. Friedrich, *Solid State Ionics*, 1998, **113–115**, 369–375.
22 W. Fischer, *Solid State Ionics*, 1999, **116**, 211–215.
23 R. Zhou, D. Wei, J. Cao, W. Feng, S. Cheng, Q. Du, B. Li, Y. Wang, D. Jia and Y. Zhou, *ACS Appl. Mater. Interfaces*, 2015, **7**, 8932–8941.
24 X. Wang, L. Mei, X. Jiang, M. Jin, Y. Xu, J. Li, X. Li, Z. Meng, J. Zhu and F. Wu, *Frontiers in Bioengineering and Biotechnology*, 2021, **9**, 625877.
25 K. Maeda, T. Motohashi, R. Ohtani, K. Sugimoto, Y. Tsuji, A. Kuwabara and S. Horike, *Sci. Technol. Adv. Mater.*, 2024, **25**, 2416384.
26 T. Kozawa, K. Yanagisawa and Y. Suzuki, *J. Ceram. Soc. Jpn.*, 2013, **121**, 308–312.
27 T. Kozawa, A. Onda and K. Yanagisawa, *J. Eur. Ceram. Soc.*, 2010, **30**, 3435–3443.
28 R. J. Paull, Z. R. Mansley, T. Ly, L. D. Marks and K. R. Poeppelmeier, *Inorg. Chem.*, 2018, **57**, 4104–4108.
29 A. C. Masset, C. Michel, A. Maignan, M. Hervieu, O. Toulemonde, F. Studer, B. Raveau and J. Hejtmanek, *Phys. Rev. B: Condens. Matter Mater. Phys.*, 2000, **62**, 166.
30 Y. Miyazaki, M. Onoda, T. Oku, M. Kikuchi, Y. Ishii, Y. Ono, Y. Morii and T. Kajitani, *J. Phys. Soc. Jpn.*, 2002, **71**, 491–497.
31 M. Isobe, M. Onoda, M. Shizuya, M. Tanaka and E. Takayama-Muromachi, *J. Am. Chem. Soc.*, 2007, **129**, 14585–14596.
32 M. Månsson, Y. Ikedo, H. Nozaki, J. Sugiyama, P. L. Russo, D. Andreica, M. Shizuya, M. Isobe and E. Takayama-Muromachi, *Solid State Commun.*, 2010, **150**, 307–310.
33 H. Yamauchi, L. Karvonen, T. Egashira, Y. Tanaka and M. Karppinen, *J. Solid State Chem.*, 2011, **184**, 64–69.
34 M. Hervieu, A. Maignan, C. Michel, V. Hardy, N. Créon and B. Raveau, *Phys. Rev. B: Condens. Matter Mater. Phys.*, 2003, **67**, 045112.
35 J. Bielecki, S. F. Parker, L. Mazzei, L. Börjesson and M. Karlsson, *J. Mater. Chem. A*, 2016, **4**, 1224–1232.
36 J. R. Martinez, C. E. Mohn, S. Stølen and N. L. Allan, *J. Solid State Chem.*, 2007, **180**, 3388–3392.
37 S. Baruah and J. Dutta, *Sci. Technol. Adv. Mater.*, 2009, **10**, 013001.
38 W. Shi, S. Song and H. Zhang, *Chem. Soc. Rev.*, 2013, **42**, 5714–5743.
39 T. Adschiri, Y. Hakuta and K. Arai, *Ind. Eng. Chem. Res.*, 2000, **39**, 4901–4907.
40 T. Adschiri, S. Takami, M. Umetsu, S. Ohara, T. Naka, K. Minami, D. Hojo, T. Togashi, T. Arita, M. Taguchi, M. Itoh, N. Aoki, G. Seong, T. Tomai and A. Yoko, *Bull. Chem. Soc. Jpn.*, 2023, **96**, 133–147.
41 E. Guilmeau, Y. Bréard and A. Maignan, *Appl. Phys. Lett.*, 2011, **99**, 052107.
42 P. Jood, M. Ohta, H. Nishiate, A. Yamamoto, O. I. Lebedev, D. Berthebaud, K. Suekuni and M. Kunii, *Chem. Mater.*, 2014, **26**, 2684–2692.
43 M. Butel, L. Gautier and C. Delmas, *Solid State Ionics*, 1999, **122**, 271–284.
44 C. S. De Matos, C. M. Ghimbeu, J. Brendlé, L. Limousy and V. R. L. Constantino, *New J. Chem.*, 2020, **44**, 16721–16732.
45 S. V. Cherepanova, N. N. Leont'Eva, A. B. Arbuzov, V. A. Drozdov, O. B. Belskaya and N. V. Antonicheva, *J. Solid State Chem.*, 2015, **225**, 417–426.
46 C. W. Mburu, S. M. Gaita, C. S. Knee, M. J. Gatari and M. Karlsson, *J. Phys. Chem. C*, 2017, **121**, 16174–16181.
47 M. Isobe, M. Onoda, M. Shizuya, M. Tanaka and E. Takayama-Muromachi, *J. Phys. Soc. Jpn.*, 2007, **76**, 014602.
48 C. Ahamer, A. K. Opitz, G. M. Rupp and J. Fleig, *J. Electrochem. Soc.*, 2017, **164**, F790–F803.
49 E. Fabbri, D. Pergolesi and E. Traversa, *Chem. Soc. Rev.*, 2010, **39**, 4355–4369.
50 N. A. Danilov, I. A. Starostina, G. N. Starostin, A. V. Kasyanova, D. A. Medvedev and Z. Shao, *Adv. Energy Mater.*, 2023, **13**, 202302175.
51 J. Wu, R. A. Davies, M. S. Islam and S. M. Haile, *Chem. Mater.*, 2005, **17**, 846–851.
52 T. B. G. Srinivas Reddy, *J. Alloys Compd.*, 2016, **688**, 1039–1046.
53 M. Khalid Hossain, R. Chanda, A. El-Denglawey, T. Emrose, M. T. Rahman, M. C. Biswas and K. Hashizume, *Ceram. Int.*, 2021, **47**, 23725–23748.
54 M. K. Hossain, M. C. Biswas, R. K. Chanda, M. H. K. Rubel, M. I. Khan and K. Hashizume, *Emergent Mater.*, 2021, **4**, 999–1027.
55 S. A. Speakman, R. D. Carneim, E. A. Payzant and T. R. Armstrong, *J. Mater. Eng. Perform.*, 2004, **13**, 303–308.
56 E. T. A. K. Ekaterina Antonova, *Ionics*, 2022, **28**, 5181–5188.
57 T. Murakami, J. R. Hester and M. Yashima, *J. Am. Chem. Soc.*, 2020, **142**, 11653–11657.
58 T. Murakami, M. Avdeev, R. Morikawa, J. R. Hester and M. Yashima, *Adv. Funct. Mater.*, 2023, **33**, 2206777.
59 S. Kawaguchi, M. Takemoto, K. Osaka, E. Nishibori, C. Moriyoshi, Y. Kubota, Y. Kuroiwa and K. Sugimoto, *Rev. Sci. Instrum.*, 2017, **88**, 085111.
60 V. Petrícek, M. Dušek and L. Palatinus, *Z. Kristallogr.*, 2014, **229**, 345–352.